

J. Rafael Pacheco

Assistant Professor,
Departamento de Ingeniería Mecánica,
Instituto Tecnológico de Monterrey,
Monterrey, NJ 64849, México
Mem. ASME,
e-mail: rpacheco@asu.edu

Arturo Pacheco-Vega

Visiting Assistant Professor,
Department of Aerospace
and Mechanical Engineering,
University of Notre Dame,
Notre Dame, IN 46556
Mem. ASME

Analysis of Thin Film Flows Using a Flux Vector Splitting¹

We propose a flux vector splitting (FVS) for the solution of film flows radially spreading on a flat surface created by an impinging jet using the shallow-water approximation. The governing equations along with the boundary conditions are transformed from the physical to the computational domain and solved in a rectangular grid. A first-order upwind finite difference scheme is used at the point of the shock while a second-order upwind differentiation is applied elsewhere. Higher-order spatial accuracy is achieved by introducing a MUSCL approach. Three thin film flow problems (1) one-dimensional dam break problem, (2) radial flow without jump, and (3) radial flow with jump, are investigated with emphasis in the prediction of hydraulic jumps. Results demonstrate that the method is useful and accurate in solving the shallow water equations for several flow conditions. [DOI: 10.1115/1.1538626]

Introduction

A phenomenon of interest in free-surface film flows under certain conditions is the formation of a sudden discontinuity in the depth of a flowing liquid; i.e., a hydraulic jump, as the flow in the radial direction makes a transition from supercritical to a subcritical regime. Significant back-flow may be present at the jump location with a corresponding loss of mechanical energy due to the abrupt change in depth. In general, the region of increased film thickness corresponds to a zone of substantially amplified turbulence. From a thermal standpoint, the location of the hydraulic jump is critical because of the degraded transport characteristics that exist there. This region is unsteady, and depends heavily on the drainage configuration downstream.

Thin film flows can be characterized as shallow-water flows in which the vertical dimension is much smaller than any typical horizontal length scale. Important applications of the shallow-water equations include the prediction of weather, simulation of tidal flows, storm surges, river flows, and dam-break waves.

For engineering applications numerical solution of the governing equations is a useful tool for aiding in the prediction of local flow properties of the fluid. From a numerical standpoint, a major difficulty in analyzing the hydraulic jump stems from the discontinuity of the fluid depth across the jump, which must be accurately captured by the numerical method.

Due to the similarity between the depth-averaged equations and the two-dimensional compressible Navier-Stokes equations, the methods developed to solve the compressible flow may also be used to study the shallow water equations and therefore to analyze hydraulic jumps in thin flows.

Several finite difference schemes have been developed for the simulation of gas dynamics equations and are available in the literature. The main difference among them is the way they address the problem of shock waves formation, which is of fundamental importance in the overall accuracy of the calculations. These techniques are based either on central-difference formulations, [1,2], or on upwind-difference discretizations. Though the earlier schemes give fairly accurate results in the case of smooth and weak-shocks, the precision given by the latter methods, even for problems containing strong shock waves, is superior, [3]. Representatives of upwind schemes are those by Roe [4] and Yee and Harten [5], based on flux difference splitting (FDS) techniques,

and those by Steger and Warming [6], van Leer [7], and Walters et al. [8] structured on the flux vector splitting (FVS) approach.

Since the shallow-water equations have the property of being nonhomogeneous functions of the primitive variables, the application of FVS schemes to the solution of these equations has been limited, mainly due to the difficulty in finding the proper split of the flux vectors. However, a number of numerical studies for the shallow-water equations using schemes based on the FDS method have been carried out. Examples include the study of flow in a channel of infinite width, [9], the simulation of open channel flows coupled with flux limiters, [10], and the analysis of two-dimensional free-surface flow equations employing a high-order Godunov-type scheme based on monotone upstream-centered scheme for conservation laws (MUSCL) variable extrapolation and slope limiters, [11], among others.

In the current work we are interested in the analysis of free-surface thin film flows, for which a hydraulic jump may exist, using the shallow water equations as mathematical model. To this end, we use a finite difference scheme based on a new split of the flux vector to solve the governing equations. A first-order upwind differentiation is enforced at the location of the shock whereas a higher order upwind differentiation is employed elsewhere. A straight forward formulation of the governing equations is presented followed by a discussion of the split of the flux vector that accounts for the inhomogeneity of the shallow-water model. The effects of the FVS on the accuracy and consistency of the spatial discretization are studied next. Finally, three thin film problems (1) one-dimensional dam break problem, (2) radial flow without jump, and (3) radial flow with jump, are investigated with emphasis in the capability of the technique to capture discontinuities in the flow field.

Mathematical Model

Governing Equations. We present the governing Navier-Stokes and continuity equations for incompressible fluid with constant properties,

$$\nabla \cdot \mathbf{u} = 0 \quad (1)$$

$$\frac{\partial \mathbf{u}}{\partial t} + \mathbf{u} \cdot \nabla \mathbf{u} = -\nabla p + \nu \nabla^2 \mathbf{u} + g \mathbf{e}_z, \quad (2)$$

where \mathbf{e}_z is the unit vector in the vertical direction; $\mathbf{u} = (u, v, w)$

¹Address correspondence to ASU, P.O. Box 6106, Tempe, AZ 85287-6106.

Contributed by the Fluids Engineering Division for publication in the JOURNAL OF FLUIDS ENGINEERING. Manuscript received by the Fluids Engineering Division December 15, 1999; revised manuscript received October 11, 2002. Associate Editor: Y. Matsumoto.

represents the Cartesian velocity vector components; p is the pressure; ν is the kinematic viscosity; ρ is the density, and g is the gravitational acceleration. In the following, the physical space will be denoted by (x, y, z) , and the computational space by (ξ, η, ζ) .

Assuming that vertical acceleration, wind stresses and Coriolis effects are negligible, the bottom slope is small, and considering that the friction losses can be computed using uniform steady flow formulas, [12], the set of equations (1)–(2) can be vertically averaged to obtain the two-dimensional unsteady shallow flow equations. The depth-averaged equations of motion can be written in conservation law form as

$$\frac{\partial \mathbf{Q}}{\partial t} + \frac{\partial \mathbf{E}}{\partial x} + \frac{\partial \mathbf{F}}{\partial y} = \mathbf{S}, \quad (3)$$

where

$$\mathbf{Q} = \begin{bmatrix} h \\ hU \\ hV \end{bmatrix}; \quad \mathbf{E} = \begin{bmatrix} hU \\ hU^2 + \frac{gh^2}{2} \\ hUV^2 \end{bmatrix}; \quad \mathbf{F} = \begin{bmatrix} hV \\ hUV \\ hV^2 + \frac{gh^2}{2} \end{bmatrix};$$

$$\mathbf{S} = \begin{bmatrix} 0 \\ -gh \frac{\partial z_b}{\partial x} - \frac{\tau_{bx}}{\rho} \\ -gh \frac{\partial z_b}{\partial y} - \frac{\tau_{by}}{\rho} \end{bmatrix}. \quad (4)$$

Here h is the water depth measured vertically, U and V are the Cartesian depth-averaged velocity components, z_b is the channel bottom elevation, t is time, g is the gravitational acceleration, and τ_{bx} and τ_{by} are the bottom shear stress components. The bottom stress is an unknown quantity in the shallow water equations and has to be expressed in terms of the other variables in order to “close” the system. In the current formulation the effective stress components are neglected and the shear stress on the bottom is approximated using the Chezy formulas

$$\tau_{bx} = \frac{g}{C^2} U(U^2 + V^2)^{1/2}, \quad \tau_{by} = \frac{g}{C^2} V(U^2 + V^2)^{1/2}, \quad (5)$$

where C is the Chezy constant, [13]. The advantage of this approach (assuming the pressure distribution to be hydrostatic), is that leads to a considerable simplification in both the mathematical formulation and the numerical solution without degrading the accuracy of the overall solution, for most engineering applications, [14].

Equation (3) can be written in generalized coordinates as

$$\frac{\partial \hat{\mathbf{Q}}}{\partial \tau} + \frac{\partial \hat{\mathbf{E}}}{\partial \xi} + \frac{\partial \hat{\mathbf{F}}}{\partial \eta} = \hat{\mathbf{S}}, \quad (6)$$

where $\hat{\mathbf{Q}}$ represents the standard form of the conserved variables. Because of the particular structure of these equations, it is possible to write

$$\frac{\partial \hat{\mathbf{E}}}{\partial \xi} = \hat{\mathbf{A}} \frac{\partial \hat{\mathbf{Q}}}{\partial \xi} \quad \text{and} \quad \frac{\partial \hat{\mathbf{F}}}{\partial \eta} = \hat{\mathbf{B}} \frac{\partial \hat{\mathbf{Q}}}{\partial \eta}, \quad (7)$$

where $\hat{\mathbf{A}}$ and $\hat{\mathbf{B}}$ are the flux Jacobian matrices, i.e., $\hat{A}_{ij} = \partial \hat{E}_i / \partial \hat{Q}_j$ and $\hat{B}_{ij} = \partial \hat{F}_i / \partial \hat{Q}_j$. The elements of Eqs. (6)–(7) are shown in the Appendix.

The system of equations (6) is hyperbolic and therefore the direction of propagation of information is determined by the sign of the eigenvalues of the Jacobian matrices, $\hat{\mathbf{A}}$ and $\hat{\mathbf{B}}$, which are all real. For $\hat{\mathbf{A}}$ and $\hat{\mathbf{B}}$ a similarity transformation exists such that $\hat{\mathbf{A}} = \hat{\mathbf{E}}_\lambda \hat{\Lambda} \hat{\mathbf{E}}_\lambda^{-1}$ and $\hat{\mathbf{B}} = \hat{\mathbf{F}}_\gamma \hat{\Gamma} \hat{\mathbf{F}}_\gamma^{-1}$, where $\hat{\Lambda}$ and $\hat{\Gamma}$ are the diagonal matrices of eigenvalues, and $\hat{\mathbf{E}}_\lambda$ and $\hat{\mathbf{F}}_\gamma$ the associated eigen-

Table 1 Boundary conditions for the shallow-water equations

Case	Condition	Number of Outward Characteristics	Number of Inward Characteristics	Number of Boundary Conditions
1	$U_c < -a\sqrt{\xi_x^2 + \xi_y^2}$	0	3	3
2	$-a\sqrt{\xi_x^2 + \xi_y^2} \leq U_c < 0$	1	2	2
3	$0 \leq U_c < a\sqrt{\xi_x^2 + \xi_y^2}$	2	1	1
4	$U_c > a\sqrt{\xi_x^2 + \xi_y^2}$	3	0	0

vectors. If we define $U_c = \xi_x U + \xi_y V$, $V_c = \eta_x U + \eta_y V$ and $a = \sqrt{gh}$, the characteristic directions in the ξ and η -coordinates, respectively, can be written as

$$\lambda_1 = U_c, \quad \lambda_{2,3} = U_c \pm a\sqrt{\xi_x^2 + \xi_y^2} \quad (8)$$

$$\gamma_1 = V_c, \quad \gamma_{2,3} = V_c \pm a\sqrt{\eta_x^2 + \eta_y^2} \quad (9)$$

where U_c and V_c are the characteristic velocities.

Boundary Conditions. The system of equations (6) cannot be solved without assigning appropriate initial and boundary conditions. For a hyperbolic system the required number of boundary conditions is related to the behavior of the characteristics. At any point on the boundary one must specify as many conditions as there are characteristic planes entering the region. The characteristic directions of propagation are given in Eqs. (8)–(9). Considering the radial velocity as positive if the flow is outward, we may have the situations shown in Table 1. Cases 1 and 4, in the table, are concerned with supercritical flow, $Fr > 1$ where $Fr = U/\sqrt{gh}$ is the Froude number. Supercritical flows do not occur very often. For the more frequent cases, 2 and 3 ($Fr < 1$), we must specify either one or two boundary conditions depending on whether the flow is directed outward or inward.

For supercritical flow ($Fr > 1$), the boundary conditions used were: (a) upstream boundary: the longitudinal velocity U , transverse velocity V and the depth h are specified and do not change during computations, and (b) downstream boundary: all the variables, i.e., U , V , and h are extrapolated from the interior points. For subcritical flow ($Fr < 1$), the corresponding boundary conditions are (a) upstream boundary: the depth h is specified and the longitudinal velocity U is extrapolated from the interior points, and (b) downstream boundary: the velocities U and V are specified and the depth h is extrapolated from the interior points.

Splitting Scheme

The splitting of the flux vectors $\hat{\mathbf{E}}$ and $\hat{\mathbf{F}}$, in Eq. (6), can be accomplished in a number of ways. The most common choice is in accord to the sign of the eigenvalues of the system, where the flux vectors can be split into subvectors. Each subvector is associated with the positive or negative eigenvalues of the flux matrix Jacobian. Thus, $\hat{\mathbf{A}}$ can be split as $\hat{\mathbf{A}} = \hat{\mathbf{A}}^+ + \hat{\mathbf{A}}^-$ where $\hat{\mathbf{A}}^+ = \hat{\mathbf{E}}_\lambda \hat{\Lambda}^+ \hat{\mathbf{E}}_\lambda^{-1}$ and $\hat{\mathbf{A}}^- = \hat{\mathbf{E}}_\lambda \hat{\Lambda}^- \hat{\mathbf{E}}_\lambda^{-1}$, where the elements of $\hat{\Lambda}^+$ and $\hat{\Lambda}^-$ are the positive and negative eigenvalues, respectively. Similarly $\hat{\mathbf{B}} = \hat{\mathbf{B}}^+ + \hat{\mathbf{B}}^-$, where $\hat{\mathbf{B}}^+ = \hat{\mathbf{F}}_\gamma \hat{\Gamma}^+ \hat{\mathbf{F}}_\gamma^{-1}$ and $\hat{\mathbf{B}}^- = \hat{\mathbf{F}}_\gamma \hat{\Gamma}^- \hat{\mathbf{F}}_\gamma^{-1}$.

In the case of the Euler equations, the fluxes associated with these Jacobians are obtained from the property of homogeneity of the flux vector $\hat{\mathbf{E}}(\hat{\mathbf{Q}})$. If the flux vector $\hat{\mathbf{E}}$ is an homogeneous function of degree one in $\hat{\mathbf{Q}}$, one has $\hat{\mathbf{E}} = \hat{\mathbf{A}}\hat{\mathbf{Q}}$. In a similar fashion, $\hat{\mathbf{F}}$ can be written as $\hat{\mathbf{F}} = \hat{\mathbf{B}}\hat{\mathbf{Q}}$. The property of homogeneity was used by Steger and Warming [6] to split the flux vector into forward and backward contributions. The eigenvalues of the Jacobian matrix of the full flux were split into non-negative and nonpositive groups. An alternate flux splitting with continuously differentiable flux contributions that lead to smoother solutions at sonic points was introduced in van Leer [7]. An important remark to be made

is that the concept of flux splitting as previously defined, is totally dependent on the fact that the fluxes are homogeneous functions of degree one in $\hat{\mathbf{Q}}$.

Although the system of equations (6) is hyperbolic and has some similarities with the Euler equations for compressible flows, there are some differences: the Jacobian matrices $\hat{\mathbf{A}}$ and $\hat{\mathbf{B}}$ of the shallow-water equations are not homogeneous functions of degree one in $\hat{\mathbf{Q}}$. Hence, the flux vectors of Eq. (6) cannot be expressed as $\hat{\mathbf{E}} = \hat{\mathbf{A}}\hat{\mathbf{Q}}$, and $\hat{\mathbf{F}} = \hat{\mathbf{B}}\hat{\mathbf{Q}}$.

It is possible to use the FVS method to solve the shallow-water equations by splitting the flux vectors $\hat{\mathbf{E}}$ and $\hat{\mathbf{F}}$ in Eq. (6) according to $\hat{\mathbf{E}} = \hat{\mathbf{E}}^+ + \hat{\mathbf{E}}^-$ and $\hat{\mathbf{F}} = \hat{\mathbf{F}}^+ + \hat{\mathbf{F}}^-$, where

$$\hat{\mathbf{E}}^+ = \tilde{\mathbf{A}}^+ \hat{\mathbf{Q}} \quad \text{and} \quad \hat{\mathbf{E}}^- = \tilde{\mathbf{A}}^- \hat{\mathbf{Q}}, \quad (10)$$

and

$$\hat{\mathbf{F}}^+ = \tilde{\mathbf{B}}^+ \hat{\mathbf{Q}} \quad \text{and} \quad \hat{\mathbf{F}}^- = \tilde{\mathbf{B}}^- \hat{\mathbf{Q}}. \quad (11)$$

To this end, we introduce the modified Jacobian matrices $\tilde{\mathbf{A}}$ and $\tilde{\mathbf{B}}$, where

$$\tilde{\mathbf{A}} = \hat{\mathbf{E}}_\lambda \tilde{\mathbf{A}} \hat{\mathbf{E}}_\lambda^{-1} \quad (12)$$

with the diagonal matrix of eigenvalues

$$\tilde{\mathbf{A}} = \begin{bmatrix} \frac{\xi_x Q_2 + \xi_y Q_3}{Q_1} & 0 & 0 \\ 0 & \frac{\xi_x Q_2 + \xi_y Q_3 + 1/2 Q_1 \sqrt{Q_1 g (\xi_x^2 + \xi_y^2)}}{Q_1} & 0 \\ 0 & 0 & \frac{\xi_x Q_2 + \xi_y Q_3 - 1/2 Q_1 \sqrt{Q_1 g (\xi_x^2 + \xi_y^2)}}{Q_1} \end{bmatrix}; \quad (13)$$

and the corresponding expression for the modified Jacobian $\tilde{\mathbf{B}}$

$$\tilde{\mathbf{B}} = \hat{\mathbf{F}}_\gamma \tilde{\mathbf{B}} \hat{\mathbf{F}}_\gamma^{-1}, \quad (14)$$

with the diagonal matrix of eigenvalues

$$\tilde{\mathbf{B}} = \begin{bmatrix} \frac{\eta_x Q_2 + \eta_y Q_3}{Q_1} & 0 & 0 \\ 0 & \frac{\eta_x Q_2 + \eta_y Q_3 + 1/2 Q_1 \sqrt{Q_1 g (\eta_x^2 + \eta_y^2)}}{Q_1} & 0 \\ 0 & 0 & \frac{\eta_x Q_2 + \eta_y Q_3 - 1/2 Q_1 \sqrt{Q_1 g (\eta_x^2 + \eta_y^2)}}{Q_1} \end{bmatrix}. \quad (15)$$

It is now possible to obtain a well-behaved solution by splitting the spatial derivatives in two parts associated with the characteristic speeds. The flux vectors can be split into subvectors, such that each subvector is associated with positive or negative eigenvalues of the modified Jacobian matrix. Therefore, $\tilde{\mathbf{A}}$ can be split according to $\tilde{\mathbf{A}} = \tilde{\mathbf{A}}^+ + \tilde{\mathbf{A}}^-$ where $\tilde{\mathbf{A}}^+ = \hat{\mathbf{E}}_\lambda \tilde{\mathbf{A}}^+ \hat{\mathbf{E}}_\lambda^{-1}$, and $\tilde{\mathbf{A}}^- = \hat{\mathbf{E}}_\lambda \tilde{\mathbf{A}}^- \hat{\mathbf{E}}_\lambda^{-1}$. The elements of the diagonal matrices $\tilde{\mathbf{A}}^+$ and $\tilde{\mathbf{A}}^-$ are the positive and negative eigenvalues of the modified Jacobian matrix. Similarly, we write for the η -coordinate $\tilde{\mathbf{B}} = \tilde{\mathbf{B}}^+ + \tilde{\mathbf{B}}^-$ where $\tilde{\mathbf{B}}^+ = \hat{\mathbf{F}}_\gamma \tilde{\mathbf{B}}^+ \hat{\mathbf{F}}_\gamma^{-1}$ and $\tilde{\mathbf{B}}^- = \hat{\mathbf{F}}_\gamma \tilde{\mathbf{B}}^- \hat{\mathbf{F}}_\gamma^{-1}$.

$\tilde{\mathbf{A}}$ and $\tilde{\mathbf{B}}$ were modified from the original eigenvalues of the Jacobians $\hat{\mathbf{A}}$ and $\hat{\mathbf{B}}$ (see the Appendix) to introduce a new splitting of the flux vectors $\hat{\mathbf{E}}$ and $\hat{\mathbf{F}}$. In a later section we will discuss the effect of modifying the characteristic speed on the consistency and accuracy of the scheme.

Discretization Schemes

The governing equations (6) are solved by marching in time from some known set of initial conditions. The general form of the time-difference approximation is given by

$$\begin{aligned} \Delta \hat{\mathbf{Q}}^{n+1} &+ \frac{\theta_1 \Delta \tau}{1 + \theta_2} \left\{ \frac{\delta}{\delta \xi} [(\hat{\mathbf{A}}^+ + \hat{\mathbf{A}}^-)^n \Delta \hat{\mathbf{Q}}^{n+1}] \right. \\ &+ \left. \frac{\delta}{\delta \eta} [(\hat{\mathbf{B}}^+ + \hat{\mathbf{B}}^-)^n \Delta \hat{\mathbf{Q}}^{n+1}] \right\} \\ &= - \frac{\Delta \tau}{1 + \theta_2} \left(\frac{\delta}{\delta \xi} [\hat{\mathbf{E}}^+ + \hat{\mathbf{E}}^-] + \frac{\delta}{\delta \eta} [\hat{\mathbf{F}}^+ + \hat{\mathbf{F}}^-] \right)^n \\ &- \frac{(1 + \theta_1) \Delta \tau}{1 + \theta_2} \hat{\mathbf{S}}^n - \frac{\theta_1 \Delta \tau}{1 + \theta_2} \hat{\mathbf{S}}^{n-1} + \frac{\theta_1}{1 + \theta_2} (\hat{\mathbf{Q}}^n - \hat{\mathbf{Q}}^{n-1}) \end{aligned} \quad (16)$$

where the difference approximations for $\delta(\hat{\mathbf{E}}^+ + \hat{\mathbf{E}}^-)/\delta \xi$ are shown in the next section. For the numerical simulations presented here, an explicit scheme is chosen ($\theta_1 = 0$ and $\theta_2 = 0$) to solve Eq. (16).

Spatial Differencing Scheme. The upwind differencing of the convective terms is based on the flux splitting technique, where the spatial derivatives of $\hat{\mathbf{E}}^+$ and $\hat{\mathbf{E}}^-$ are approximated with backward and forward difference operators, respectively. Combining the standard first and second-order backward/forward differences the spatial derivatives can be expressed as

$$\left(\frac{\delta \hat{\mathbf{E}}^+(\mathbf{Q})}{\delta \xi}\right)_i = \frac{(\hat{\mathbf{E}}_i^+ - \hat{\mathbf{E}}_{i-1}^+)}{\Delta \xi} + \frac{\phi_i^-(\hat{\mathbf{E}}_i^+ - \hat{\mathbf{E}}_{i-1}^+)}{2\Delta \xi} - \frac{\phi_{i-1}^-(\hat{\mathbf{E}}_{i-1}^+ - \hat{\mathbf{E}}_{i-2}^+)}{2\Delta \xi} \quad (17)$$

and

$$\left(\frac{\delta \hat{\mathbf{E}}^-(\mathbf{Q})}{\delta \xi}\right)_i = \frac{(\hat{\mathbf{E}}_{i+1}^- - \hat{\mathbf{E}}_i^-)}{\Delta \xi} + \frac{\phi_i^+(\hat{\mathbf{E}}_{i+1}^- - \hat{\mathbf{E}}_i^-)}{2\Delta \xi} - \frac{\phi_{i+1}^+(\hat{\mathbf{E}}_{i+2}^- - \hat{\mathbf{E}}_{i+1}^-)}{2\Delta \xi}. \quad (18)$$

Equation (17) can also be written as

$$\left(\frac{\delta \hat{\mathbf{E}}^+(\mathbf{Q})}{\delta \xi}\right)_i = \frac{\hat{\mathbf{E}}_{i+1/2}^+ - \hat{\mathbf{E}}_{i-1/2}^+}{\Delta \xi} \quad (19)$$

with

$$\hat{\mathbf{E}}_{i+1/2}^+ = \hat{\mathbf{E}}_i^+ - \frac{\phi_i^-}{2}(\hat{\mathbf{E}}_i^+ - \hat{\mathbf{E}}_{i-1}^+); \quad (20)$$

which is equivalent to obtaining the value of $\hat{\mathbf{E}}$ at the center of the cell followed by a forward extrapolation. The parameter ϕ appearing in Eqs. (17)–(18) limits the higher-order terms by acting as a nonlinear switch. ϕ enhances shock capturing by dropping from a second-order to a first-order scheme near discontinuities so that oscillations in large gradient regions such as in the vicinity of a shock are suppressed. The spatial differencing is second-order for $\phi=1$ and first-order for $\phi=0$. The value of ϕ is determined locally from

$$\phi = \left[\frac{2\|\Delta_\xi \mathbf{Q}_i \nabla_\xi \mathbf{Q}_i\| + \epsilon}{(\Delta_\xi \mathbf{Q}_i)^2 + (\nabla_\xi \mathbf{Q}_i)^2 + \epsilon} \right]^n \quad (21)$$

where ϵ is a small number $O(10^{-6})$, [8], and n is a positive number ($0 < n \leq 1$) used to capture the shock profile. The operators Δ_ξ and ∇_ξ are the standard forward and backward difference operators, respectively.

A spatial-discretization alternative is first, to extrapolate nodal point values of $\hat{\mathbf{Q}}$ toward the face of the cell, and then to obtain $\hat{\mathbf{E}}^\pm$ at the interfaces. This is implemented as a flux balance across the cell and leads to the following approximation:

$$\left(\frac{\delta \hat{\mathbf{E}}(\hat{\mathbf{Q}})}{\delta \xi}\right)_i = \frac{[\hat{\mathbf{E}}^+(\hat{\mathbf{Q}}_{i+1/2}^-) - \hat{\mathbf{E}}^+(\hat{\mathbf{Q}}_{i-1/2}^-) + \hat{\mathbf{E}}^-(\hat{\mathbf{Q}}_{i+1/2}^+) - \hat{\mathbf{E}}^-(\hat{\mathbf{Q}}_{i-1/2}^+)]}{\Delta \xi} \quad (22)$$

where $\hat{\mathbf{E}}^\pm(\hat{\mathbf{Q}}^\mp)$ denotes $\hat{\mathbf{E}}^\pm$ evaluated at $\hat{\mathbf{Q}}^\mp$, and

$$\hat{\mathbf{Q}}_{i+1/2, j}^- = \hat{\mathbf{Q}}_{i, j} + \frac{\phi_i^-}{4}[(1 - \kappa \phi_i^-) \nabla_\xi + (1 + \kappa \phi_i^-) \Delta_\xi] \tilde{\mathbf{Q}}_{i, j} \quad (23)$$

$$\hat{\mathbf{Q}}_{i+1/2, j}^+ = \hat{\mathbf{Q}}_{i+1, j} - \frac{\phi_{i+1}^+}{4}[(1 + \kappa \phi_{i+1}^+) \Delta_\xi + (1 - \kappa \phi_{i+1}^+) \nabla_\xi] \hat{\mathbf{Q}}_{i+1, j}. \quad (24)$$

The aforementioned method, developed by van Leer [7], is often referred as the MUSCL-type approach. In Eqs. (23)–(24), κ determines the spatial accuracy of the difference approximation. For fully upwind differencing, the choice $\kappa = -1$ is used whereas $\kappa = 1/3$ corresponds to the upwind-biased third-order scheme, [15,16]. Analogous expressions to (17)–(22) may be obtained for the gradient of the fluxes $\delta(\mathbf{F}^+ + \hat{\mathbf{F}}^-)/\delta \eta$.

A comparison of numerical results for the dam-break problem, obtained with the discretized forms of Eqs. (17)–(18), and Eq. (22) will be presented in the section of numerical experiments.

Accuracy and Consistency Analyses. We now analyze the impact on the order of accuracy and consistency of the scheme due to the modification of the characteristic speeds (eigenvalues) of the modified Jacobian matrices $\tilde{\tilde{\mathbf{A}}}$ and $\tilde{\tilde{\mathbf{B}}}$ of our flux-splitting.

Consider for simplicity the one-dimensional shallow-water equation

$$\frac{\partial \hat{\mathbf{Q}}}{\partial \tau} + \frac{\partial \hat{\mathbf{E}}^+}{\partial \xi} + \frac{\partial \hat{\mathbf{E}}^-}{\partial \xi} = 0 \quad (25)$$

discretized in space and time with the following first-order scheme as

$$\begin{aligned} \hat{\mathbf{Q}}_i^{n+1} - \hat{\mathbf{Q}}_i^n &= -\frac{\Delta \tau}{\Delta \xi} [(\hat{\mathbf{E}}_i^+ - \hat{\mathbf{E}}_{i-1}^+) + (\hat{\mathbf{E}}_{i+1}^- - \hat{\mathbf{E}}_i^-)]^n \\ &= -\frac{\Delta \tau}{\Delta \xi} [(\hat{\mathbf{E}}_i^+ + \hat{\mathbf{E}}_{i+1}^-) - (\hat{\mathbf{E}}_{i-1}^+ + \hat{\mathbf{E}}_i^-)]^n. \end{aligned} \quad (26)$$

On expressing the absolute value of $\hat{\mathbf{E}}$ as $|\hat{\mathbf{E}}| = \hat{\mathbf{E}}^+ - \hat{\mathbf{E}}^- = |\tilde{\tilde{\mathbf{A}}}| \hat{\mathbf{Q}}$, where $|\tilde{\tilde{\mathbf{A}}}| = \hat{\mathbf{E}}_\lambda |\tilde{\tilde{\mathbf{A}}}| \hat{\mathbf{E}}_\lambda^{-1}$, and using $\hat{\mathbf{E}} = \tilde{\tilde{\mathbf{A}}}^+ \hat{\mathbf{Q}} + \tilde{\tilde{\mathbf{A}}}^- \hat{\mathbf{Q}}$ with $\tilde{\tilde{\mathbf{A}}}^+ \hat{\mathbf{Q}} = \hat{\mathbf{E}}^+$ and $\tilde{\tilde{\mathbf{A}}}^- \hat{\mathbf{Q}} = \hat{\mathbf{E}}^-$, we can recast Eq. (26) as

$$\begin{aligned} \hat{\mathbf{Q}}_i^{n+1} - \hat{\mathbf{Q}}_i^n &= -\frac{\Delta t}{2\Delta \xi} (\hat{\mathbf{E}}_{i+1} - \hat{\mathbf{E}}_{i-1})^n \\ &+ \frac{\Delta \tau}{2\Delta \xi} (|\hat{\mathbf{E}}|_{i+1} - 2|\hat{\mathbf{E}}|_i + |\hat{\mathbf{E}}|_{i-1})^n, \end{aligned} \quad (27)$$

to show an artificial viscosity term proportional to the second derivative of the absolute flux value $|\hat{\mathbf{E}}|$. It can be noticed from Eq. (27) that the consistency of the scheme is maintained.

After a Taylor expansion of $(|\hat{\mathbf{E}}|_{i+1} - |\hat{\mathbf{E}}|_i)$ and $(|\hat{\mathbf{E}}|_i - |\hat{\mathbf{E}}|_{i-1})$, we can transform Eq. (27) in a form that explicits the absolute value of the modified Jacobian $|\tilde{\tilde{\mathbf{A}}}|$; e.g.,

$$|\hat{\mathbf{E}}|_{i+1} - |\hat{\mathbf{E}}|_i = |\tilde{\tilde{\mathbf{A}}}|_{i+(1/2)} (\hat{\mathbf{Q}}_{i+1} - \hat{\mathbf{Q}}_{i-1}) + O(\Delta \xi) (\hat{\mathbf{Q}}_{i+1} - \hat{\mathbf{Q}}_{i-1}), \quad (28)$$

$$|\hat{\mathbf{E}}|_i - |\hat{\mathbf{E}}|_{i-1} = |\tilde{\tilde{\mathbf{A}}}|_{i-(1/2)} (\hat{\mathbf{Q}}_{i+1} - \hat{\mathbf{Q}}_{i-1}) + O(\Delta \xi) (\hat{\mathbf{Q}}_{i+1} - \hat{\mathbf{Q}}_{i-1}). \quad (29)$$

Using Eqs. (28)–(29), Eq. (27) becomes, to the first-order accuracy

$$\begin{aligned} \hat{\mathbf{Q}}_i^{n+1} - \hat{\mathbf{Q}}_i^n &= -\frac{\Delta t}{2\Delta \xi} (\hat{\mathbf{E}}_{i+1} - \hat{\mathbf{E}}_{i-1})^n + \frac{\Delta \tau}{2\Delta \xi} [|\tilde{\tilde{\mathbf{A}}}|_{i+(1/2)} (\hat{\mathbf{Q}}_{i+1} - \hat{\mathbf{Q}}_i) \\ &- |\tilde{\tilde{\mathbf{A}}}|_{i-(1/2)} (\hat{\mathbf{Q}}_i - \hat{\mathbf{Q}}_{i-1})]^n + O(\Delta \hat{\mathbf{Q}}^2). \end{aligned} \quad (30)$$

Equations (26) and (27) are equivalent formulations of the first-order conservative upwind scheme (25) for smooth variations of \hat{Q} . One can write Eq. (26) in terms of the numerical flux, as

$$\hat{Q}_i^{n+1} - \hat{Q}_i^n = -\frac{\Delta \tau}{\Delta \xi} (\hat{E}_{i+1/2} - \hat{E}_{i-1/2})^n \quad (31)$$

with $\hat{E}_{i+1/2} = \hat{E}_i^+ + \hat{E}_{i+1}^-$, or up to second-order accuracy as

$$\hat{E}_{i+1/2} = \frac{1}{2} (\hat{E}_i + \hat{E}_{i+1}) - \frac{1}{2} \tilde{A}_{i+(1/2)} (\hat{Q}_{i+1} - \hat{Q}_i) + O(\Delta \hat{Q}^2). \quad (32)$$

It can be observed that the modification of the characteristic speed does not affect the order of accuracy of the scheme, as it is part of an artificial dissipation term [16].

Numerical Experiments

Three problems are solved in order to examine the proposed FVS. The first is the analysis of the well-known one-dimensional

dam-breaking, the second corresponds to a radial flow within a supercritical region in the domain for which no hydraulic jump exists, and the third is a radial flow in the presence of supercritical and subcritical regions which induce a hydraulic jump.

One-Dimensional Dam-Breaking Problem. This problem consists of a dam located at the origin ($x=0$) in a rectangular channel, that extends to $\pm\infty$, in which fluid is initially at rest on both sides. The x -coordinate is in the downstream direction of the channel. The initial height of the fluid on the left ($x<0$) is 1 m while the height on the right ($x>0$) is 0.8 m. For this problem, [17] developed an exact solution based on the theory of characteristics to analyze the behavior of the fluid after the dam breaks. The numerical simulations were carried out using the proposed FVS along with four different schemes: a first-order upwind, a second-order upwind, and two different schemes that use slope limiters.

Figures 1(a)–1(d) illustrate comparisons of the results obtained from the numerical procedure with the exact solution at time t

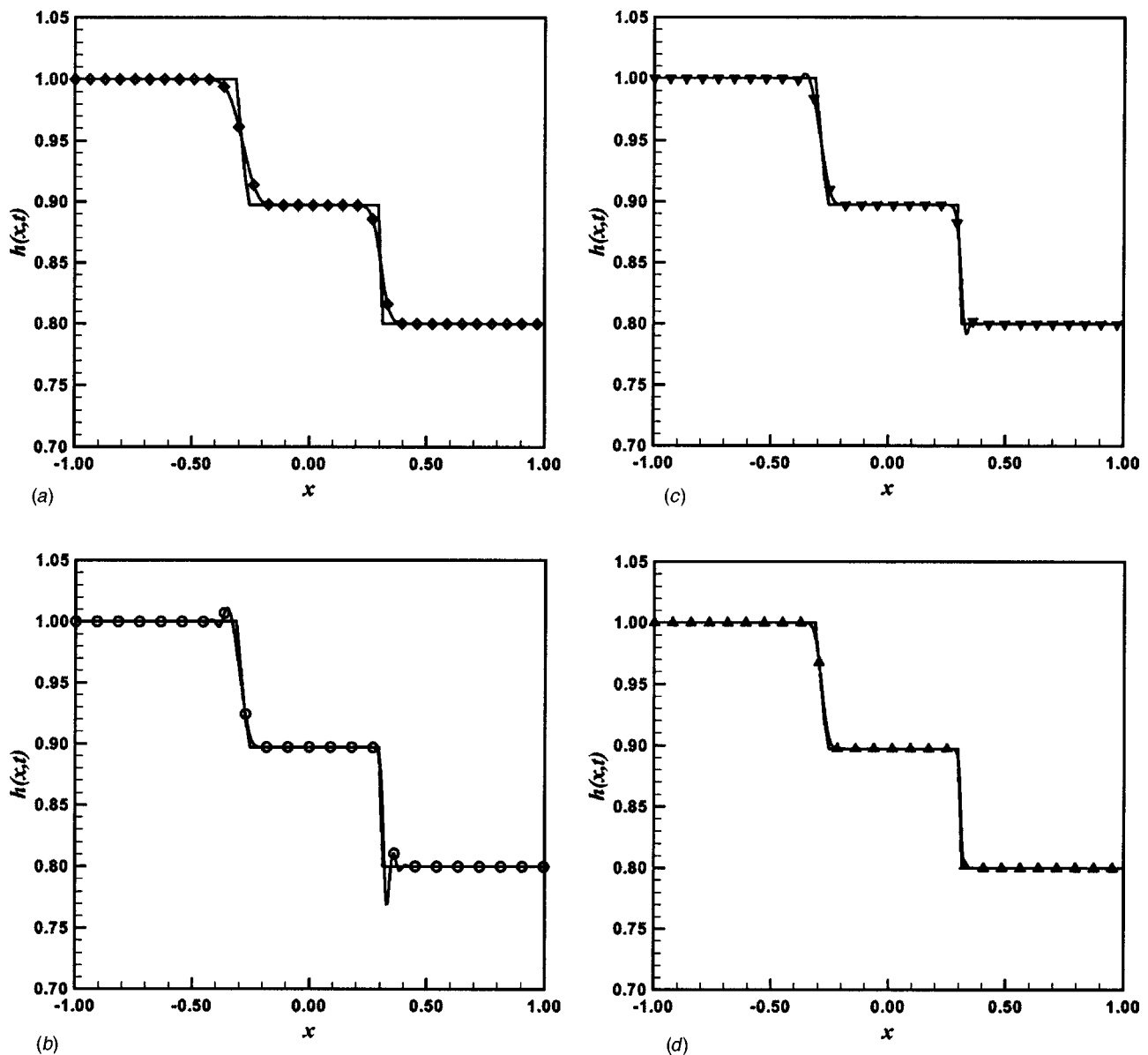


Fig. 1 Water depth of the dam-break problem in a rectangular channel at time $t=0.10$ second and 440 grid points. (a) Exact solution; $-\diamond-$ first-order scheme. (b) Exact solution; $-\circ-$ second-order scheme. (c) Exact solution; $-\nabla-$ scheme based on flux extrapolation \hat{E} with limiter. (d) Exact solution; $-\triangle-$ scheme based on variable extrapolation \hat{Q} (MUSCL) with limiter.

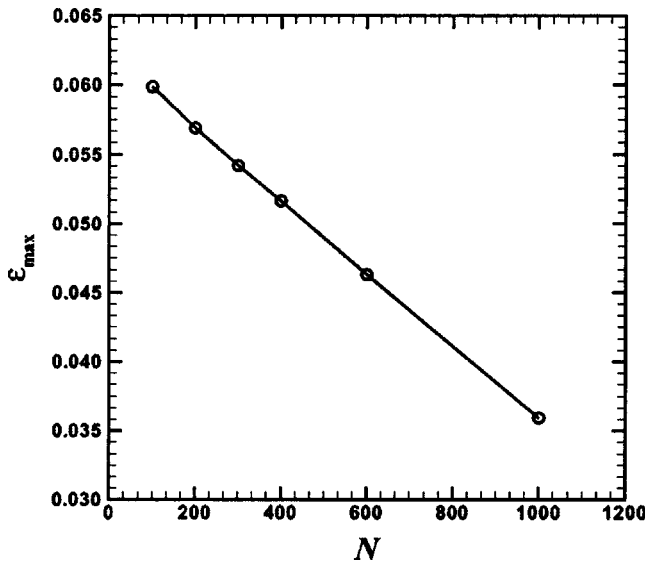


Fig. 2 Maximum relative error of h as a function of mesh refinement for the dam-break problem on a rectangular channel at time $t=0.10$ s at the points of discontinuity

$=0.10$ seconds using 440 mesh points. It can be observed from the figures that, in general, the discontinuities are captured by all the schemes, but some differences in accuracy are evident. For instance, Fig. 1(a) shows that the first-order upwind scheme has good properties of monotonicity, however it suffers from severe inaccuracies because of the high level of truncation error. On the other hand, the second-order upwind scheme, shown in Fig. 1(b), yields low levels of numerical dissipation, but steep gradients produce an oscillating behavior due to its numerical dispersion. In Fig. 1(c) the slope limiter technique based on extrapolation of the flux vector \hat{E} shows a substantial reduction in the amplitude of the oscillations at the discontinuities but cannot be completely suppressed. Finally, the results obtained from coupling FVS with the MUSCL technique indicate that the method is able to capture the discontinuities in a sharp way, avoiding any unrealistic oscillation as illustrated in Fig. 1(d).

The maximum relative error in h , ϵ_{\max} , at the points of discontinuity and time of 0.10 s is plotted in Fig. 2 as a function of mesh refinement, for the MUSCL scheme. Similar results were obtained for the velocity U . A uniform grid was used in the computation. The time-step was refined proportional to the grid spacing. Figure 2 shows that the present method is first-order accurate at the shock locations. The maximum relative error in h at time 0.10 s away from the shock is presented in Table 2 as function of mesh refinement. The experimentally established orders or accuracy are also shown in this table as function of mesh refinement. In our computation, we used $\kappa=1/3$ which corresponds to the upwind-biased third-order scheme, [15].

Radial Flow Without Jump. We simulate the radial flow with the proposed flux vector splitting method coupled with the MUSCL technique and compare the results with the experiments

Table 2 Convergence test results for the dam-break problem away from the discontinuity region

N	ϵ_{\max} (m)	Order
100	-	-
200	$2.25893928 \times 10^{-5}$	1.9716
300	$8.58939347 \times 10^{-6}$	2.3847
400	$3.58939360 \times 10^{-6}$	3.0327

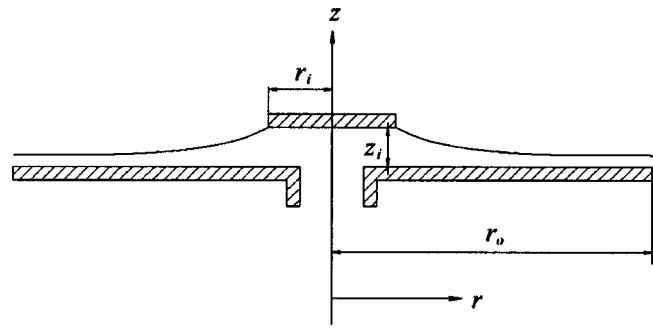


Fig. 3 Schematic of the experiment layout of Sadler and Higgins [18]

of Sadler and Higgins [18]. A layout of their experimental setup is shown in Fig. 3; the reported geometrical parameters and flow rates are presented in Table 3 as case 1. It consists of a 2.44 m (8 ft) square sheet of Plexiglas mounted horizontally on a 15.2 cm (6 in) diameter vertical pipe. Both Plexiglas and pipe were fixed to a structure. Water was discharged from a nozzle, from below, onto a 20.3 cm (8 in) diameter disk located at a height of 5 mm (3/16 in) above the sheet of Plexiglas. The water was then collected through a series of drains arranged in a circular fashion located at a distance of 68.6 cm (27 in) from the center. In the experiment, the depth of the flow was measured with a point gauge mounted on an arm under steady-state conditions.

For simulation purposes, we use a flow rate of $Q_w = 0.0098 \text{ m}^3/\text{s}$ (0.345 cfs), as reported by Sadler and Higgins [18], and a value of the Chezy constant $C=80$, [19], which is in the range commonly used for practical engineering calculations. It must be noted that a simplification of the problem can be obtained since the flow is axisymmetric, so that a one-dimensional version of the shallow-water equations in cylindrical coordinates may be used. Nonetheless, we consider a two-dimensional discretization

Table 3 Conditions from experiments for the solution of the shallow-water equations

Case	r_i (m)	r_o (m)	z_i (m)	Q_w (m^3/s)	Experiment
1	0.102	0.686	5×10^{-3}	0.0098	Sadler and Higgins [18]
2	0.082	0.914	8×10^{-3}	0.0170	Ahmad [21]

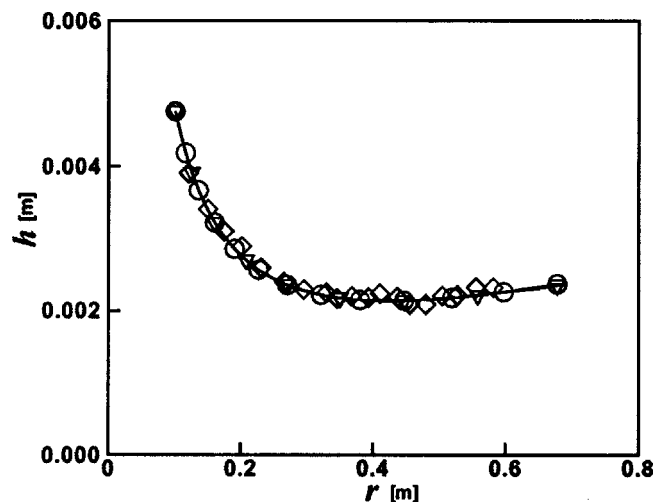


Fig. 4 Comparison of numerical solutions and experiments for $Q_w=0.0098 \text{ m}^3/\text{s}$ (0.345 cfs); ∇ - (121 \times 121) grid points; \circ - (241 \times 241) grid points; \diamond Sadler and Higgins [18]

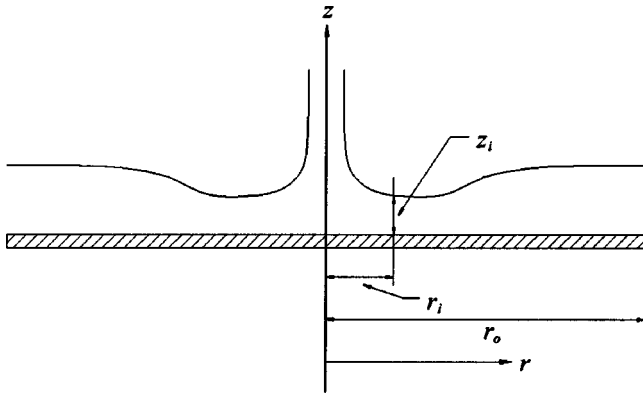


Fig. 5 Schematic of the experiment layout of Ahmad [21]

of the domain in order to illustrate potential applications of the method for nonaxisymmetric flows, [20]. The upstream values of h , U , and V are assigned as initial conditions for the numerical runs at all the grid points. The upstream boundary condition is of the Dirichlet type (case 1 of Table 1). Since the flow is supercritical within the domain, the boundary condition downstream corresponds to the Neumann type. Therefore the values of the variables are extrapolated using the values at the interior points. In the azimuthal direction periodic boundary conditions were implemented. The numerical scheme was tested until grid independent solutions were obtained by successively refining the mesh. Figure 4 shows the film height for two different sets of mesh points. The FVS-based model was run until steady state was reached.

A comparison between the numerical calculations obtained from the proposed FVS method and the experimental results of Sadler and Higgins [18] is presented in Fig. 4. The water surface profiles determined from the model and the surface profile found experimentally for the current analysis are shown in this figure. The numerical results display a very good agreement with experiments.

Radial Flow With Jump. The radially spreading flow of a thin liquid film is simulated in the presence of supercritical and subcritical regions. The shock-capturing capabilities of our FVS method are tested and the results are compared with the laboratory test data obtained by [21]. A schematic of the experimental layout is shown in Fig. 5. It consisted of a 2.14 m (7 ft) diameter by 2.5 cm (1 in) thickness circular plywood disc placed in a circular steel

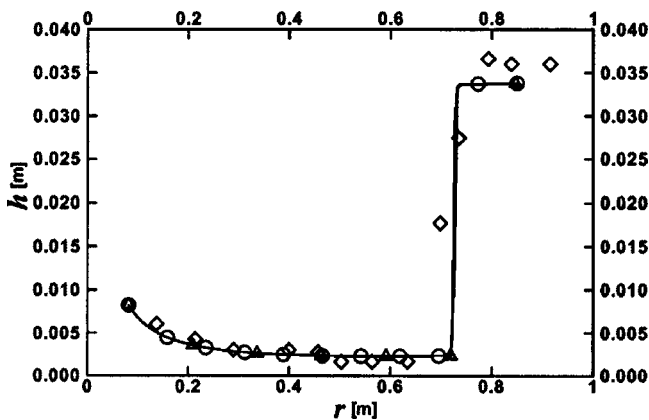


Fig. 6 Comparison of water surface profile of a hydraulic jump for $Q_w=0.0170 \text{ m}^3/\text{s}$ (0.60 cfs) between experiments and numerical solutions for different number of grid points: $-\triangle-$ (121 \times 121) grid mesh; $-\circ-$ (241 \times 121) grid mesh; \diamond observed by Ahmad [21]

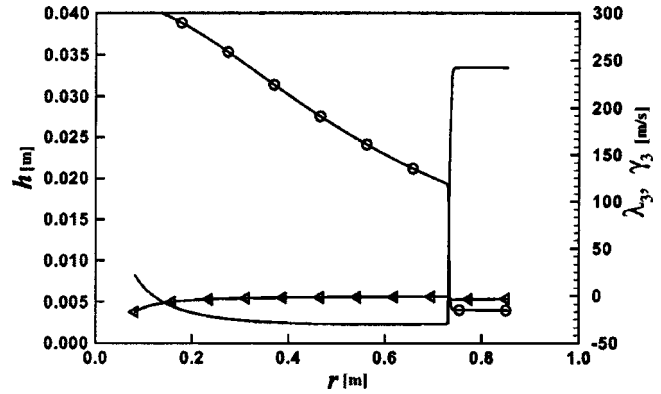


Fig. 7 Evolution of the eigenvalues and appearance of the hydraulic jump; $-\circ-$ λ_3 ; $-\triangle-$ γ_3 ; $-$ height h . FVS with slope limiter solution; (241 \times 121) grid points.

tank of diameter 2.29 m (7.5 ft). A ring of 1.83 m (6 ft) inside diameter, 2.14 m (7 ft) outside diameter, and 2.5 cm (1 in) thickness was placed on the plywood disk to control the downstream depth and consequently the location of the jump. A 10.2 cm (4 in) diameter pipe was used to convey the water onto the disc. The distance between the nozzle and the disc was kept at 2 cm (13/16 in).

For the numerical simulation we use the flow conditions reported by Ahmad [21] which are presented as case 2 in Table 3. Since the flow is supercritical in the upstream region, the variables U , V , and h , once specified, remain unchanged during the iteration process. At the downstream boundary, U and V are defined whereas h is extrapolated from the interior points. Periodic boundary conditions are prescribed in the azimuthal direction. For the present case, the value of the Chezy constant was chosen as $C=90$, [19], and the time-step $\Delta\tau$ was restricted to a CFL=0.5. Results from this run are shown in Fig. 6. The values of the speed of propagation (eigenvalues λ_3 and γ_3) are shown in Fig. 7 as a function of the radial position. From Fig. 7, it is clear that the change of sign of the eigenvalue λ_3 coincides with the location of the jump, as expected. It is also important to note that the location of the jump coincides at a location where the characteristics intersect. In our test, we start from an initial condition and stop the computation when the change in water depth reaches a prescribed tolerance of $\epsilon=1.0 \times 10^{-5}$ m.

The computed results from the proposed scheme and the measurements of Ahmad [21] are shown in Fig. 6 for comparison. From the figure it can be observed first that the film heights from the simulations using a mesh of 121 \times 121 points, are almost identical when increasing the number of grid points in the radial-azimuthal directions to 241 \times 121, for the same initial conditions indicating grid independence. Moreover, when comparing the numerical simulations with the experimental measurements becomes clear that the method simulates the supercritical flow accurately, and that it is able to determine the location of the jump. The sharp transition from supercritical to subcritical flow is clearly shown in Fig. 6. In the region of transition from supercritical to subcritical flow, the computed water-depth magnitude is very close to the measured height reported in the experiment. In the subcritical region where the flow is turbulent, the difference in heights between simulations and experiments becomes larger. These differences may be due on one side to experimental uncertainties which are increased in the turbulent region, and on the other, to the energy dissipated at the location of the jump, which is not accounted for in the shallow-water formulation.

Concluding Remarks

The hydraulic jump is an intriguing complex phenomenon commonly found in nature. The complexity stems from the change in

the character of the flow at the jump location with the corresponding production of distorted free surfaces and flow separation. Because of its important role in engineering applications, e.g., the design of water courses, energy dissipators, etc., it is crucial to determine accurately the characteristics of the jump such as position and thickness.

The shallow water equations are mathematically similar to the equations for compressible fluid flow. They are useful in predicting the location of shocks, at which the height of the free surface and the mean fluid velocity are discontinuous. In contrast to the compressible fluid flow equations, the shallow water equations do not possess the property of homogeneity and hence common FVS cannot be used to solve them. In this work we have introduced a new FVS that allows the analysis of thin film flows, in particular, the formation of hydraulic jumps within the flow domain using the shallow-water theory. The proposed splitting of the flux vectors was obtained by modified Jacobian matrices that account for the inhomogeneity of the system. Details of the methodology and theoretical analyses have been included to illustrate its implementation, consistency and accuracy.

The usefulness of the proposed FVS is tested by coupling the method to several finite difference schemes, two of them with slope limiters, that yield high-order accuracy away from the location of the shock. The numerical predictions have shown favorable comparisons with the theoretical solution of the dam-break problem. When the proposed FVS is used in conjunction with MUSCL, the resulting scheme is more efficient and produces accurate results in the location of the discontinuity and the height of the flow, avoiding unrealistic oscillations. An excellent agreement with laboratory experiments and analytical solutions confirmed the efficiency of the method. The technique proposed here has been successfully applied to analyze axisymmetric and nonaxisymmetric density currents, [20].

Acknowledgments

The authors would like to thank Prof. Kyle Squires for helpful discussions on this work and to Prof. Miguel Angel Arredondo of

Universidad Iberoamericana, León, for access to computer facilities. We are grateful for the helpful comments of the anonymous referees which improved the quality of the manuscript.

Appendix

Expanded Vectors. We present next the expanded form of the expressions often encountered in solving the shallow-water equations. The flux vectors are given by

$$\hat{\mathbf{Q}} = \frac{1}{J} \begin{bmatrix} Q_1 \\ Q_2 \\ Q_3 \end{bmatrix} = \frac{1}{J} \begin{bmatrix} h \\ hU \\ hV \end{bmatrix} \quad (33)$$

$$\hat{\mathbf{E}} = \frac{1}{J} \begin{bmatrix} \xi_x Q_2 + \xi_y Q_3 \\ \frac{\xi_x Q_2^2 + \xi_y Q_2 Q_3}{Q_1} + \frac{\xi_x}{2} g Q_1^2 \\ \frac{\xi_x Q_2 Q_3 + \xi_y Q_3^2}{Q_1} + \frac{\xi_y}{2} g Q_1^2 \end{bmatrix} \quad (34)$$

$$\hat{\mathbf{F}} = \frac{1}{J} \begin{bmatrix} \eta_x Q_2 + \eta_y Q_3 \\ \frac{\eta_x Q_2^2 + \eta_y Q_2 Q_3}{Q_1} + \frac{\eta_x}{2} g Q_1^2 \\ \frac{\eta_x Q_2 Q_3 + \eta_y Q_3^2}{Q_1} + \frac{\eta_y}{2} g Q_1^2 \end{bmatrix} \quad (35)$$

$$\hat{\mathbf{S}} = \frac{1}{J} \begin{bmatrix} 0 \\ -g Q_1 \frac{\partial z_b}{\partial x} - \frac{g}{C^2} \frac{Q_2}{Q_1^2} \sqrt{Q_2^2 + Q_3^2} \\ -g Q_1 \frac{\partial z_b}{\partial y} - \frac{g}{C^2} \frac{Q_3}{Q_1^2} \sqrt{Q_2^2 + Q_3^2} \end{bmatrix} \quad (36)$$

The Jacobians of flux vectors are

$$\hat{\mathbf{A}} = \frac{\partial \hat{\mathbf{E}}}{\partial \hat{\mathbf{Q}}} = \begin{bmatrix} 0 & \xi_x & \xi_y \\ -\frac{\xi_x Q_2^2 + \xi_y Q_2 Q_3 - g Q_1^3}{Q_1^2} & \frac{2\xi_x Q_2 + \xi_y Q_3}{Q_1} & \frac{\xi_y Q_2}{Q_1} \\ -\frac{\xi_x Q_2 Q_3 + \xi_y Q_3^2 - g Q_1^3}{Q_1^2} & \frac{\xi_x Q_3}{Q_1} & \frac{\xi_x Q_2 + 2\xi_y Q_3}{Q_1} \end{bmatrix} \quad (37)$$

The diagonal matrix of eigenvalues is

$$\hat{\mathbf{\Lambda}} = \begin{bmatrix} \frac{\xi_x Q_2 + \xi_y Q_3}{Q_1} & 0 & 0 \\ 0 & \frac{\xi_x Q_2 + \xi_y Q_3 + Q_1 \sqrt{Q_1 g (\xi_x^2 + \xi_y^2)}}{Q_1} & 0 \\ 0 & 0 & \frac{\xi_x Q_2 + \xi_y Q_3 - Q_1 \sqrt{Q_1 g (\xi_x^2 + \xi_y^2)}}{Q_1} \end{bmatrix} \quad (38)$$

and the corresponding set of eigenvectors can be written as

$$\hat{\mathbf{E}}_\lambda = \begin{bmatrix} 0 & 1 & 1 \\ \xi_y & \frac{Q_2}{Q_1} + \frac{\xi_x \sqrt{(\xi_x^2 + \xi_y^2) g Q_1}}{(\xi_x^2 + \xi_y^2)} & \frac{Q_2}{Q_1} - \frac{\xi_x \sqrt{(\xi_x^2 + \xi_y^2) g Q_1}}{(\xi_x^2 + \xi_y^2)} \\ -\xi_x & \frac{Q_3}{Q_1} + \frac{\xi_y \sqrt{(\xi_x^2 + \xi_y^2) g Q_1}}{(\xi_x^2 + \xi_y^2)} & \frac{Q_3}{Q_1} - \frac{\xi_y \sqrt{(\xi_x^2 + \xi_y^2) g Q_1}}{(\xi_x^2 + \xi_y^2)} \end{bmatrix} \quad (39)$$

The inverse of the left eigenvectors is expressed as

$$\hat{\mathbf{E}}_{\lambda}^{-1} = \begin{bmatrix} -\frac{Q_2 \xi_y - \xi_x Q_3}{Q_1(\xi_x^2 + \xi_y^2)} & \frac{\xi_y}{(\xi_x^2 + \xi_y^2)} & -\frac{\xi_x}{(\xi_x^2 + \xi_y^2)} \\ -\frac{\xi_y Q_3 - Q_1 \sqrt{(\xi_x^2 + \xi_y^2)gQ_1} + \xi_x Q_2}{2Q_1 \sqrt{(\xi_x^2 + \xi_y^2)gQ_1}} & \frac{\xi_x}{2\sqrt{(\xi_x^2 + \xi_y^2)gQ_1}} & \frac{\xi_y}{2\sqrt{(\xi_x^2 + \xi_y^2)gQ_1}} \\ \frac{\xi_y Q_3 + Q_1 \sqrt{(\xi_x^2 + \xi_y^2)gQ_1} + \xi_x Q_2}{2Q_1 \sqrt{(\xi_x^2 + \xi_y^2)gQ_1}} & -\frac{\xi_x}{2\sqrt{(\xi_x^2 + \xi_y^2)gQ_1}} & -\frac{\xi_y}{2\sqrt{(\xi_x^2 + \xi_y^2)gQ_1}} \end{bmatrix}. \quad (40)$$

The Jacobians of flux vectors are

$$\hat{\mathbf{B}} = \frac{\partial \hat{\mathbf{F}}}{\partial \hat{\mathbf{Q}}} = \begin{bmatrix} 0 & \eta_x & \eta_y \\ -\frac{\eta_x Q_2^2 + \eta_y Q_2 Q_3 - gQ_1^3}{Q_1^2} & \frac{2\eta_x Q_2 + \eta_y Q_3}{Q_1} & \frac{\eta_y Q_2}{Q_1} \\ -\frac{\eta_x Q_2 Q_3 + \eta_y Q_3^2 - gQ_1^3}{Q_1^2} & \frac{\eta_x Q_3}{Q_1} & \frac{\eta_x Q_2 + 2\eta_y Q_3}{Q_1} \end{bmatrix}. \quad (41)$$

The diagonal matrix form of the Jacobians of flux vectors can be written as

$$\hat{\mathbf{\Gamma}} = \begin{bmatrix} \frac{\eta_x Q_2 + \eta_y Q_3}{Q_1} & 0 & 0 \\ 0 & \frac{\eta_x Q_2 + \eta_y Q_3 + Q_1 \sqrt{Q_1 g(\eta_x^2 + \eta_y^2)}}{Q_1} & 0 \\ 0 & 0 & \frac{\eta_x Q_2 + \eta_y Q_3 - Q_1 \sqrt{Q_1 g(\eta_x^2 + \eta_y^2)}}{Q_1} \end{bmatrix}. \quad (42)$$

The set of eigenvectors corresponding to the eigenvalues is

$$\hat{\mathbf{F}}_y = \begin{bmatrix} 0 & 1 & 1 \\ \eta_y & \frac{Q_2}{Q_1} + \frac{\eta_x \sqrt{(\eta_x^2 + \eta_y^2)gQ_1}}{(\eta_x^2 + \eta_y^2)} & \frac{Q_2}{Q_1} - \frac{\eta_x \sqrt{(\eta_x^2 + \eta_y^2)gQ_1}}{(\eta_x^2 + \eta_y^2)} \\ -\eta_x & \frac{Q_3}{Q_1} + \frac{\eta_y \sqrt{(\eta_x^2 + \eta_y^2)gQ_1}}{(\eta_x^2 + \eta_y^2)} & \frac{Q_3}{Q_1} - \frac{\eta_y \sqrt{(\eta_x^2 + \eta_y^2)gQ_1}}{(\eta_x^2 + \eta_y^2)} \end{bmatrix}. \quad (43)$$

The inverse of the set of eigenvectors is

$$\hat{\mathbf{F}}_y^{-1} = \begin{bmatrix} -\frac{Q_2 \eta_y - \eta_x Q_3}{Q_1(\eta_x^2 + \eta_y^2)} & \frac{\eta_y}{(\eta_x^2 + \eta_y^2)} & -\frac{\eta_x}{(\eta_x^2 + \eta_y^2)} \\ -\frac{\eta_y Q_3 - Q_1 \sqrt{(\eta_x^2 + \eta_y^2)gQ_1} + \eta_x Q_2}{2Q_1 \sqrt{(\eta_x^2 + \eta_y^2)gQ_1}} & \frac{\eta_x}{2\sqrt{(\eta_x^2 + \eta_y^2)gQ_1}} & \frac{\eta_y}{2\sqrt{(\eta_x^2 + \eta_y^2)gQ_1}} \\ \frac{\eta_y Q_3 + Q_1 \sqrt{(\eta_x^2 + \eta_y^2)gQ_1} + \eta_x Q_2}{2Q_1 \sqrt{(\eta_x^2 + \eta_y^2)gQ_1}} & -\frac{\eta_x}{2\sqrt{(\eta_x^2 + \eta_y^2)gQ_1}} & -\frac{\eta_y}{2\sqrt{(\eta_x^2 + \eta_y^2)gQ_1}} \end{bmatrix}. \quad (44)$$

In order to show that the shallow-water equations do not have the property of homogeneity we write

$$(\hat{\mathbf{E}}_{\lambda} \hat{\mathbf{\Lambda}} \hat{\mathbf{E}}_{\lambda}^{-1}) \hat{\mathbf{Q}} = \frac{1}{J} \begin{bmatrix} \xi_x Q_2 + \xi_y Q_3 \\ \frac{\xi_x Q_2^2 + \xi_y Q_2 Q_3}{Q_1} + \xi_x g Q_1^2 \\ \frac{\xi_x Q_2 Q_3 + \xi_y Q_3^2}{Q_1} + \xi_y g Q_1^2 \end{bmatrix} \quad (45)$$

$$(\hat{\mathbf{F}}_y \hat{\mathbf{\Gamma}} \hat{\mathbf{F}}_y^{-1}) \hat{\mathbf{Q}} = \frac{1}{J} \begin{bmatrix} \eta_x Q_2 + \eta_y Q_3 \\ \frac{\eta_x Q_2^2 + \eta_y Q_2 Q_3}{Q_1} + \eta_x g Q_1^2 \\ \frac{\eta_x Q_2 Q_3 + \eta_y Q_3^2}{Q_1} + \eta_y g Q_1^2 \end{bmatrix}, \quad (46)$$

which are different from (34) and (35).

Nomenclature

$\hat{\mathbf{A}}, \hat{\mathbf{B}}$	= Jacobian matrices
$\tilde{\mathbf{A}}, \tilde{\mathbf{B}}$	= modified Jacobian matrices
$\hat{\mathbf{A}}^+, \hat{\mathbf{B}}^+$	= Jacobians corresponding to positive eigenvalues
$\hat{\mathbf{A}}^-, \hat{\mathbf{B}}^-$	= Jacobians corresponding to negative eigenvalues
a	= speed of propagation (m/s)
C	= Chezy constant
$\mathbf{E}, \mathbf{F}, \mathbf{Q}, \mathbf{S}$	= vectors in the physical domain
$\hat{\mathbf{E}}, \hat{\mathbf{F}}, \hat{\mathbf{Q}}, \hat{\mathbf{S}}$	= vectors in the computational domain
$\hat{\mathbf{E}}^+, \hat{\mathbf{F}}^+$	= split flux vector corresponding to positive eigenvalues
$\hat{\mathbf{E}}^-, \hat{\mathbf{F}}^-$	= split flux vector corresponding to negative eigenvalues
$\hat{\mathbf{E}}_\lambda, \hat{\mathbf{F}}_\gamma$	= matrices of corresponding eigenvectors
\mathbf{e}_z	= unit vector in the vertical direction
Fr	= Froude number
g	= gravitational acceleration (m/s ²)
h	= film height (m)
J	= Jacobian
N	= number of cells
p	= pressure (N/m ²)
Q_i	= components of the depth-averaged variables (m/s)
Q_w	= volumetric flow rate (m ³ /s)
r_i	= radial location of initial measurements (m)
r_o	= outer radius of the disk (m)
t, τ	= time (s)
U, V	= depth averaged velocities (m/s)
U_c, V_c	= characteristic velocities (m/s)
\mathbf{u}	= Cartesian velocity vector (m/s)
u, v, w	= velocity components in the x, y, z -directions (m/s)
x, y, z	= Cartesian coordinates (m)
z_b	= reference height (m)
z_i	= initial film height in experiments (m)

Greek Symbols

γ, λ	= eigenvalues of the Jacobian (m/s)
δ, Δ, ∇	= finite difference operators
ϵ	= error
ϕ	= nonlinear limiting parameter
$\hat{\mathbf{\Lambda}}, \hat{\mathbf{\Gamma}}$	= diagonal matrices of eigenvalues
$\hat{\mathbf{\Lambda}}^+, \hat{\mathbf{\Gamma}}^+$	= diagonal matrices of positive eigenvalues
$\hat{\mathbf{\Lambda}}^-, \hat{\mathbf{\Gamma}}^-$	= diagonal matrices of negative eigenvalues
$\tilde{\mathbf{\Lambda}}, \tilde{\mathbf{\Gamma}}$	= diagonal matrices of modified eigenvalues
ν	= kinematic viscosity (m ² /s)
ρ	= density of the fluid (kg/m ³)
θ_1, θ_2	= weight function
τ_{bx}, τ_{by}	= bottom shear stresses (N/m ²)
ξ, η, ζ	= curvilinear coordinates (m)

Subscripts and Superscripts

i, j, k	= index for the Cartesian coordinates x, y, z
max	= maximum
n	= index of time-step

x	= x -direction, first derivative in the x -direction
y	= y -direction, first derivative in the y -direction
z	= z -direction
+	= positive eigenvalues
-	= negative eigenvalues

Abbreviations

CFL	= Courant-Friedrich-Levy number
cfs	= cubic feet per second
FVS	= flux vector splitting
FDS	= flux difference splitting
MUSCL	= monotone upstream-centered scheme for conservation laws

References

- [1] MacCormack, R. W., 1969, "The Effect of Viscosity in Hypervelocity Impact Craterings," AIAA Paper No. 69-354.
- [2] Beam, R. M., and Warming, R. F., 1976, "An Implicit Finite-Difference Algorithm for Hyperbolic Systems in Conservation Law Form," *Comput. Phys.*, **22**, pp. 87-110.
- [3] Yee, H. C., 1989, "A Class of High-Resolution Explicit and Implicit Shock-Capturing Methods," technical report, von Karman Institute for Fluid Dynamics.
- [4] Roe, P. L., 1981, "Approximate Riemann Solvers, Parameter Vectors, and Difference Schemes," *Comput. Phys.*, **43**, pp. 357-372.
- [5] Yee, H. C., and Harten, A., 1987, "Implicit TVD Schemes for Hyperbolic Conservation-Laws in Curvilinear Coordinates," *AIAA J.*, **25**, pp. 266-274.
- [6] Steger, J. L., and Warming, R. F., 1979, "Flux Vector Splitting of the Inviscid Gasdynamic Equation With Application to Finite Difference Methods," technical report, NASA TM-78605.
- [7] Van Leer, B., 1982, "Flux-Vector Splitting for the Euler Equations," Krause E., editor, *Lecture Notes in Physics*, E. Krause, ed., Springer, Berlin, **170**, pp. 507-512.
- [8] Walters, R. W., Thomas, J. L., and Van Leer, B., 1986, "An Implicit Flux-Split Algorithm for the Compressible Euler and Navier-Stokes Equations," *Lecture Notes in Physics*, F. G. Zhuang and Y. L. Zhu, eds., Springer, Berlin, **264**, pp. 628-635.
- [9] Glaister, P., 1988, "Approximate Riemann Solutions of the Shallow Water Equations," *J. Hydraulic Res.*, **26**, pp. 293-306.
- [10] Glaister, P., 1993, "Flux Difference Splitting for Open-Channel Flows," *Int. J. Numer. Methods Fluids*, **16**, pp. 629-654.
- [11] Alcrudo, F., and Garcia-Navarro, P., 1993, "A High-Resolution Godunov-Type Scheme in Finite Volumes for the 2D Shallow-Water Equations," *Int. J. Numer. Methods Fluids*, **16**, pp. 489-505.
- [12] Chapman, R. S., and Kuo, C. Y., 1985, "Application of the Two-Equation κ - ϵ Turbulence Model to a Two-Dimensional, Steady, Free Surface Flow Problem With Separation," *Int. J. Numer. Methods Fluids*, **5**, pp. 257-268.
- [13] Vreugdenhil, C. B., 1993, *Numerical Methods for Shallow-Water Flows*, Kluwer, Dordrecht, Netherlands.
- [14] Cunge, J., 1975, "Rapidly Varying Flow in Power and Pumping Canals," *Unsteady flow in open channels*, K. Mahmood and V. Yevjevich, eds., Water Resources Publications, Littleton, CO, pp. 539-586.
- [15] Thomas, J. L., and Walters, R. W., 1985, "Upwind Relaxation Algorithms for the Navier-Stokes Equations," AIAA Paper No. 85-1501.
- [16] Hirsch, C., 1990, *Numerical Computation of Internal and External Flows*, John Wiley and Sons, New York.
- [17] Stoker, J. J., 1957, *Water Waves*, Wiley Interscience, New York.
- [18] Sadler, C. D., and Higgins, M. S., 1963, "Radial Free Surfaces Flows," master's thesis, Massachusetts Institute of Technology, Cambridge, MA.
- [19] Younus, M., and Chaudhry, M. H., 1994, "A Depth-Averaged κ - ϵ Turbulence Model for the Computation of Free Surface Flow," *J. Hydraul Res.*, **32**(3), pp. 415-444.
- [20] Hunt, J. C. R., Pacheco, J. R., Mahalov, A., and Fernando, H. J. S., 2003, "Effects of Rotation and Sloping Terrain on Fronts of Density Currents," *J. Fluid Mech.*, (submitted).
- [21] Ahmad, D., 1967, "Circular Hydraulic Jump," master's thesis, Colorado State University, Fort Collins, CO.